Wideband Josephson Parametric Isolator

M.A. Beck,* M. Selvanayagam, A. Carniol, S. Cairns, and C.P. Mancini
IBM Quantum, IBM T. J. Watson Research Center, Yorktown Heights, New York 10598, USA

(Received 20 December 2022; revised 26 June 2023; accepted 7 August 2023; published 22 September 2023)

The cryogenic hardware required to build a superconducting-qubit-based quantum computer demands a variety of microwave components. These elements include microwave couplers, filters, amplifiers, and circulators and/or isolators. Traditionally implemented as discrete components, integration of this peripheral hardware, in an effort to reduce overall footprint, thermal load, and added noise, is a key challenge to scaling modern quantum processors with qubit counts climbing over the one hundred plus mark. Ferrite-based microwave isolators, generally employed in the readout chain to decouple qubits and resonators from readout electronics, persist as one of the volumetrically largest devices still utilized as discrete components. Here, we present an alternative two-port isolating integrated circuit derived from the dc superconducting quantum interference device (dc SQUID). Nonreciprocal transmission is achieved using the three-wave microwave-mixing properties of a flux-modulated dc SQUID. We show that when multiple dc SQUIDs are embedded in a multipole admittance-inverting filter structure, the three-wave mixing derived from the flux pumping of the dc SQUIDs can provide directional microwave power flow. For a three-pole filter device, we experimentally demonstrate a directionality greater than 15 dB over a 600-MHz bandwidth.

DOI: 10.1103/PhysRevApplied.20.034054

I. INTRODUCTION

The readout of superconducting quantum processing units (QPUs) is generally performed by dispersively coupling linear microwave resonators to individual qubits [1–3]. Determination of the qubit states is achieved via the application of a weak ($P \approx -120$ dBm) microwave probe tone to the linear resonator, where the qubit state is mapped to a phase shift of the probe tone. This probe tone and its corresponding phase shift are then amplified, demodulated, and digitized at room temperature.

In many state-of-the-art QPU designs, multiplexed readout of multiple resonators is achieved via a common coupled transmission line [3–5]. In-band noise or signals emanating back toward the QPU from downstream readout electronics can introduce spurious photon populations to the quantum readout resonators, leading to excess dephasing [6,7]. Modern systems generally decouple the QPU from this downstream noise via commercial ferrite-based cryogenic microwave isolators with single-junction devices achieving greater than 20 dB of in-band isolation. Often, systems will serially cascade multiple devices in an effort to increase the overall isolation and thus prevent degradation of QPU performance.

As a consequence of their large physical footprint, placing numerous isolators at the mixing chamber of a dilution refrigerator to support increasing qubit counts is a daunting system-integration challenge. In an effort to meet the future demands of larger quantum systems, integrated-circuit approaches toward realizing an isolator replacement are an active area of research [8]. Recently, the inherent nonlinear inductance of Josephson junctions (JJs) has been utilized to realize nonreciprocal behavior [9]. Numerous JJ-based devices have been proposed, building off existing amplifier designs, including nonreciprocal devices derived from Josephson parametric amplifiers (JPAs) [10], Josephson ring modulators (JRMs) [11–14], traveling-wave devices [15,16], and other circuit topologies [17]. In addition, robust theoretical models of nonreciprocal time-varying JJ-based circuits have been developed based on multimode modeling and graph theory [14,18,19].

In this paper, we present our work on the development of cryogenic wideband isolators utilizing SQUIDs as a nonlinear mixing element. We present this work in seven sections. Building on the works detailed in Refs. [8,19], Sec. II analyzes a generalized case of the parametrically pumped LC circuits utilizing coupled-mode theory [19]. We derive analytical expressions for the observed directionality D as a function of the pump strength, the pump frequency, and the differential pump phase. In Sec. III, we demonstrate how rf flux modulation of a dc SQUID gives rise to a spectral impedance matrix, where one can directly calculate the three- and four-wave mixing products. We further show how the employment of two or more rf flux pumped dc SQUIDs can give rise to constructive and destructive interference depending on the differential flux modulation phase between two SQUIDs that are capacitively coupled. Section III concludes by

*matthew.beck@ibm.com

$$M = \begin{bmatrix} \Delta_{A_1} & \beta_{A_1A_2} & \beta_{A_1B_1} & 0 & \beta_{A_1C_1} & 0 \\ \beta_{A_2A_1} & \Delta_{A_2} & 0 & \beta_{A_2B_2}e^{i\phi} & 0 & \beta_{A_2C_2}e^{-i\phi} \\ \beta_{B_1A_1} & 0 & \Delta_{B1} & \beta_{B_1B_2} & 0 & 0 \\ 0 & \beta_{B_2A_2}e^{-i\phi} & \beta_{B_2B_1} & \Delta_{B_2} & 0 & 0 \\ \beta_{C_1A_1} & 0 & 0 & 0 & \Delta_{C_1} & \beta_{C_1C_2} \\ 0 & \beta_{C_2A_2}e^{i\phi} & 0 & 0 & \beta_{C_2C_1} & \Delta_{C_2} \end{bmatrix}, \tag{1}$$

comparing spectral ABCD and harmonic balance simulations of a three-pole admittance inverting filter with embedded flux modulated dc SQUIDs. Sections IV and V detail the fabrication and measurements of superconducting wideband parametric isolators utilizing flux-modulated dc SQUIDs, respectively. Sections VI and VII describe paths for future work and conclusions.

II. COUPLED-MODE ISOLATING FILTER

Admittance-inverting filters are a useful tool in the development of wideband superconducting parametric devices, finding use in the development of rf switches [20], amplifiers [21], and IQ mixers [22]. In this section, we utilize coupled-mode theory [18,19,23] to investigate the dynamics of a two-pole admittance inverting filter circuit in which the resonant frequency of each pole is modulated via an rf pump. Figure 1(a) displays a diagram of the circuit. We note that the following treatment is agnostic as to the physical implementation of the nonlinearity, i.e., whether the shunt inductor or shunt capacitor of the pole [8] embodies the nonlinear component subject to modulation. However, as described later, we will look at an implementation of a filter where the shunt inductor is replaced with a dc SQUID. In Secs. II A and II B, we focus on a two-pole admittance inverting filter topology and look to understand the constraints on the pump parameters, including the relative phase between pumps, the pump frequency, and the pump amplitude required to realize nonreciprocal transmission.

A. Determining the pump parameters

We employ a two-pole band-pass filter as our model, as shown in Fig. 1(a). In order to capture the dynamics arising solely from the first upper and lower sidebands generated due to the pole frequency modulation, an equivalent coupled-mode network comprised of six distinct modes is utilized. A diagram of the network is shown in Fig. 1(b). The A modes are at the center frequency of the filter ω_o, the B modes are at upper sideband $\omega_B = \omega_o + \omega_p$, and the C modes are at the lower sideband $\omega_C = \omega_o - \omega_p$, where ω_p is the pump frequency. Thus the B and C modes are simply the first two sidebands generated via the pole nonlinearity, which are detuned from the center frequency by the pump. The coupling-matrix formulation of the graph in Fig. 1 is given in Eq. (1). Where $\Delta_X = 1/\gamma_0\left(\omega_X^s - \omega_X + i\gamma_X/2\right)$ encapsulates the detuning of the mode ω_X from the applied signal frequency ω_X^s. The γ_X term represents the coupling between the mode and the external ports. The leading term $\gamma_0 = \sqrt[N]{\Pi_{n=1}^{N}\gamma_i}$ is the geometric mean loss rate for the coupled-mode system. The β_{XY} terms describe the coupling between modes X and Y. Double-line connections represent parametric coupling between modes and single-line connections represent passive coupling [19]. Sidebands linked to the center frequency via parametric couplings are defined by the modulation amplitude and phase. We make the coupling phase explicit via a differential phase offset term ϕ between modes B_2 and A_2 and modes C_2 and A_2 so as to provide the required degree of freedom to create constructive and destructive interference.

To calculate the required differential phase, we take the limit where the input and output coupling are equal, $\gamma_i = \gamma_o = \gamma_0$, and the signal frequency is equal to the A mode. In this limit, Eq. (1) reduces to

$$M = \begin{bmatrix} i/2 & \beta_c & \beta_p & 0 & \beta_p & 0 \\ \beta_c & i/2 & 0 & \beta_p e^{i\phi} & 0 & \beta_p e^{-i\phi} \\ \beta_p & 0 & i/2 + \omega_p/\gamma_0 & \beta_c & 0 & 0 \\ 0 & \beta_p e^{-i\phi} & \beta_c & i/2 + \omega_p/\gamma_0 & 0 & 0 \\ \beta_p & 0 & 0 & 0 & i/2 - \omega_p/\gamma_0 & \beta_c \\ 0 & \beta_p e^{i\phi} & 0 & 0 & \beta_c & i/2 - \omega_p/\gamma_0 \end{bmatrix}, \tag{2}$$

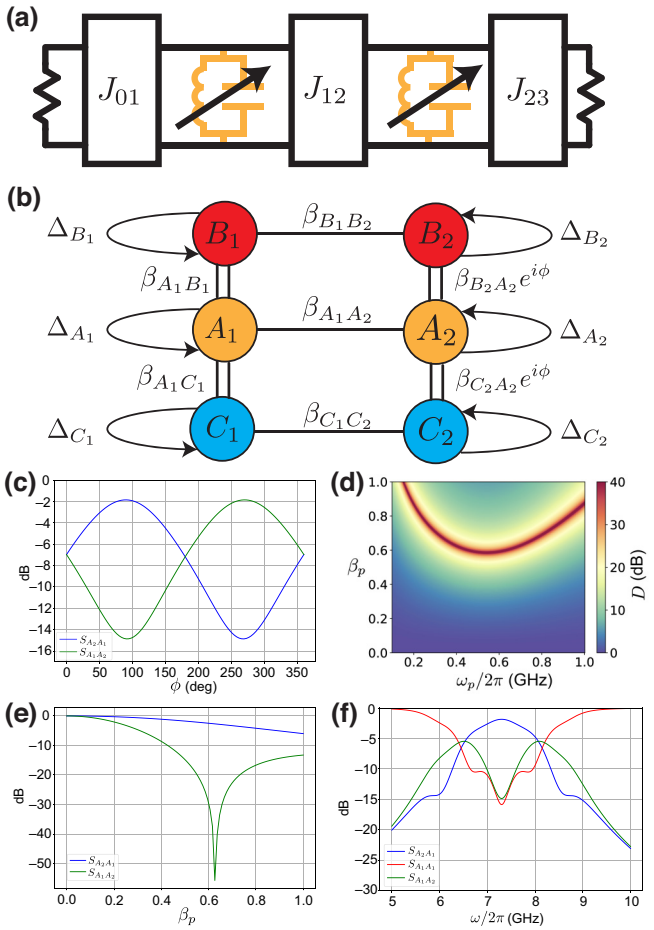

FIG. 1. (a) The two-pole bandpass admittance inverting filter diagram with modulated LC resonances. (b) The coupled-mode graph equivalent of (a). (c) Forward $S_{A_2A_1}$ and reverse $S_{A_1A_2}$ transmission as a function of the differential flux pump phase ϕ. (d) A false-color plot of the directionality D as a function of the pump frequency ω_p and the pump strength β_p for a phase $\phi = \pi/2$. (e) The forward and reverse scattering parameters as a function of the pump strength β_p. (f) The forward, reflected, and reverse scattering parameters for the coupled-mode diagram in (b) for a pump strength $\beta_p = 0.5$ and a differential pump phase $\phi = \pi/2$.

where we have set the coupling rates between degenerate frequencies $\beta_{X_1X_2} = \beta_c$ and the parametric couplings $\beta_{X_NY_N} = \beta_p$. To calculate the directionality, we invert Eq. (2) and take the ratio of the forward- and reverse-coupling terms:

$$D = \frac{|S_{A_2A_1}|}{|S_{A_1A_2}|} = \frac{|M^{-1}_{A_2A_1}|}{|M^{-1}_{A_1A_2}|} \tag{3a}$$

$$= \frac{|M_a + \zeta\cos(\phi) - \eta\sin(\phi)|}{|M_a + \zeta\cos(\phi) + \eta\sin(\phi)|}, \tag{3b}$$

where

$$M_a = -\frac{\beta_c}{16} - \frac{\beta_c^3}{2} - \beta_c^5 - \frac{\beta_c\omega_p^2}{2\gamma_0^2} + \frac{2\beta_c^3\omega_p^2}{\gamma_0^2} - \frac{\beta_c\omega_p^4}{\gamma_0^4}, \tag{4}$$

$$\zeta = \frac{1}{2}\beta_c\beta_p^2 + 2\beta_c^3\beta_p^2 - 2\frac{\beta_c\beta_p^2\omega_p^2}{\gamma_0^2}, \tag{5}$$

$$\eta = 2\frac{\beta_c\beta_p^2\omega_p}{\gamma_0}. \tag{6}$$

Upon inspection of Eq. (3b), we see that for $\phi = n\pi$ (where n is an integer), $D = 1$ for any and all values related to the pump, thus yielding matching forward- and reverse-scattering amplitudes. When $\phi = (n + 1/2)\pi$, the amount of directionality depends on the ratio M_a/η, with infinite directionality (complete suppression of $S_{A_1A_2}$) achieved when $M_a/\eta = 1$. For this case, we derive two limits on the pump amplitude as a function of the pump frequency. In both cases, we take $\beta_c \ll 1$. In the limit $a \equiv \omega_p/\gamma_0 \ll 1$, the pump amplitude $\beta_p \propto \sqrt{1/a}$ for infinite directionality. In the opposite limit, $a \gg 1$, the pump amplitude $\beta_p \propto \sqrt{a^3}$.

Given the above, we can also say a few words regarding the insertion loss. In the limit $\beta_c^r\beta_p^s \ll 1$, where $r + s \geq 3$, we can derive a qualitative relation between the forward transmission and the pump amplitude. In this limit, the forward transmission takes the form

$$|S_{A_2A_1}| \approx \frac{1 + \beta_p^2}{1 + b\beta_p^2}, \tag{7}$$

where b is a numerical factor greater than 1. With the pump turned off, $|S_{A_2A_1}| = 1$, yielding unity transmission. In the limit of increasing β_p, the transmission asymptotically approaches $|S_{A_2A_1}| \to 1/b$.

We numerically calculate the forward and reverse scattering parameters via the conversion of the two-pole network in Fig. 1(a) to the equivalent coupled-mode structure in Fig. 1(b). Our model has a center frequency $\omega_A = 7.3$ GHz, a band-pass ripple $r = 0.1$ dB, and a bandwidth BW = 750 MHz. Figure 1(c) displays $S_{A_1A_2}$ and $S_{A_2A_1}$ as a function of the differential pump phase for a signal drive applied to modes A_1 and A_2 with $\beta_p = 0.5$. At differential phases $\phi = n\pi$, the simulations show $S_{A_1A_2} = S_{A_2A_1}$, resulting in unity directionality as predicted by Eq. (3b). The maximum difference is seen at $\phi = \pi/2$. Figure 1(d) plots the directionality D in decibels in false color as a function of the pump frequency ω_p and the pump strength β_p. The color bar is artificially cut off at 40 dB. The nonlinear red line displays when the denominator of Eq. (3b) goes to 0, resulting in full suppression of $S_{A_1A_2}$. Figure 1(e) plots $S_{A_2A_1}$ and $S_{A_1A_2}$ as a function of the pump strength β_p for a pump frequency $\omega_p/2\pi = 700$ MHz. The simulations show that while

exponential suppression of $S_{A_1A_2}$ is possible as one approaches a pump amplitude $\beta_p \approx 0.62$, a trade-off is made between the maximum suppression of $S_{A_1A_2}$ and the additive insertion loss in $S_{A_2A_1}$ stemming from the stiffened pump shown in Eq. (7). This additional insertion loss is due to imperfect constructive interference resulting in power lost to the sideband-mode external couplings. Figure 1(f) plots the forward-, reflected-, and reverse-scattering parameters for the coupled-mode filter for a pump amplitude $\beta_p = 0.5$. We see a suppression of $S_{A_1A_2}$ of approximately 15 dB with a corresponding insertion loss of 2 dB. An important aspect of this plot is that it predicts that the system stays matched to better than 10 dB, indicating that the nominal matched response of the underlying linear filter is maintained while under modulation. This allows us to treat the pump as a perturbative parameter to the overall circuit performance.

B. Bounding the pump frequency

Referring again to Figs. 1(a) and 1(b) and the resulting calculation, when one inserts the forms for the lower- and upper-sideband frequencies for perfect tuning, all terms on the diagonal of Eq. (1) become functions of the applied signal frequency ω_A^s and the A mode frequency ω_A *only*, providing little insight into exactly what pump frequency one should apply in an integrated broadband filter circuit. For discrete modes, the answer is simply that the pump should be the difference between the signal and the respective sideband mode frequencies. In a continuous-band circuit, what exactly constitutes a discrete mode is slightly more complicated.

To gain insight into what sets the pump frequency in a broadband circuit, we take the case in which the applied signal frequency is at the center of the filter band, $\omega_A^s = \omega_o$. We also define the isolation bandwidth $\delta\omega$ centered on ω_0, which represents the frequency bandwidth of the desired directionality for the circuit under modulation. Note that this is separate from the linear filter bandwidth BW and that, in general, $\delta\omega \leq$ BW. Two points in the continuous-signal frequency band are considered, $\omega_o + \delta\omega/2$ and $\omega_o - \delta\omega/2$, which are the upper and lower edges of the isolation bandwidth. Under modulation, both of these frequencies generate lower and upper sidebands, ω_{B+}, ω_{C+} and ω_{B-}, ω_{C-}, for a given pump frequency ω_P. These are defined as

$$\omega_B+ = \omega_A + \frac{\delta\omega}{2} + \omega_P, \tag{8}$$

$$\omega_C+ = \omega_A + \frac{\delta\omega}{2} - \omega_P, \tag{9}$$

$$\omega_B- = \omega_A - \frac{\delta\omega}{2} + \omega_P, \tag{10}$$

$$\omega_C- = \omega_A - \frac{\delta\omega}{2} - \omega_P. \tag{11}$$

Depending on the value of ω_p, only ω_{B-} and ω_{C+} will fall into the $\omega_A \pm \delta\omega/2$ band, while ω_{B+} and ω_{C-} always exist outside of it. By bounding ω_P such that ω_{B+} and ω_{C-} land outside of $\omega_A \pm \delta\omega/2$, we can get an approximate value for the pump frequency. Subtracting Eq. (9) from Eq. (10) yields

$$\omega_{B-} - \omega_{C+} = 2\omega_P - \delta\omega \geq \delta\omega, \tag{12}$$

$$\omega_P \geq \delta\omega. \tag{13}$$

By setting the pump frequency larger than the desired isolation bandwidth $\delta\omega$, we ensure that no sideband frequencies arising from the modulation lie within the isolation band. Further, we can approximately bound the pump frequency from above by noting that for frequencies ω_{B+} and ω_{C-}, which would lie outside the filter passband for large ω_P, their participation via their coupling to the filter is greatly reduced once they are largely detuned from the modes of the filter [19]. Thus, in general, keeping $\omega_P \leq$ BW suffices as a good rule, although we note that this is not a hard bound.

In practice, once a desired isolation bandwidth is chosen, flexibility exists in choosing the pump frequency. A good rule of thumb is to have $\delta\omega \lessapprox \omega_P \lessapprox$ BW, with the goal of maximizing $\delta\omega$. The smaller that $\delta\omega$ can be set with respect to the underlying linear filter bandwidth, the greater freedom there is in choosing ω_P.

III. SUPERCONDUCTING-CIRCUIT IMPLEMENTATION

With the above coupled-mode treatment detailing the rise of nonreciprocity in a modulated two-pole LC network, we propose the use of dc SQUIDs as the nonlinear mixing element. In this section, we describe how, under the application of rf flux, dc SQUIDs give rise to three- or four-wave mixing and detail how the application of two or more rf flux pumped dc SQUIDs can give rise to directionality in a two-port circuit. We conclude the section by comparing the results of a spectral ABCD matrix calculation with that of a numerical harmonic balance simulation for a three-pole admittance-inverting filter with dc SQUIDs embedded in each of the shunt LC poles.

A. dc SQUID mixer theory

A dc SQUID is comprised of the parallel combination of two JJs in a superconducting loop [24]. The dc SQUID possesses an inherent inductance with a nonlinear dependence on the flux applied through the loop. The form of the inductance is

$$L_{\mathrm{SQ}} = \frac{\Phi_0}{2\pi I_c \cos(\pi\Phi_A/\Phi_0)}, \tag{14}$$

where $\Phi_0 \equiv h/2e$ is the superconducting magnetic flux quantum, $I_c \equiv 2 \times I_{c0}$ is twice the critical current (I_{c0}) of the individual JJs, and Φ_A is the flux applied through the dc SQUID loop. Setting $\pi\Phi_A/\Phi_0 = \beta + \alpha\cos(\omega_m t + \phi)$, where β and α are the dc and rf flux amplitudes, ω_m is the modulation frequency, and ϕ is the modulation phase, we Taylor expand the $\cos(\pi\Phi_A/\Phi_0)$ about β, yielding

$$\cos(\pi\Phi_A/\Phi_0) \approx \cos(\beta) - \sin(\beta)\left(\frac{\pi\Phi_A}{\Phi_0} - \beta\right) - \frac{\cos(\beta)}{2}\left(\frac{\pi\Phi_A}{\Phi_0} - \beta\right)^2. \tag{15}$$

Making the substitution $\pi\Phi_A/\Phi_0 - \beta = \alpha\cos(\omega_m t + \phi)$, Eq. (15) can be rewritten as

$$\cos(\pi\Phi_A/\Phi_0) \approx \cos(\beta)\left[1 - \tan(\beta)\alpha\cos(\omega_m t + \phi) - \alpha^2\cos^2(\omega_m t + \phi)/2\right]. \tag{16}$$

In the small rf pump limit $\alpha \to 0$, Eq. (14) becomes

$$L_{SQ}(t) \approx \frac{\Phi_0}{4\pi I_{c0}\cos(\beta)}[1 + \tan(\beta)\alpha\cos(\omega_m t + \phi) + \alpha^2\cos^2(\omega_m t + \phi)/2]. \tag{17}$$

Finally, expanding the cos and $\cos^2$ terms into their respective exponential forms yields

$$L_{SQ}(t) \approx \frac{\Phi_0}{4\pi I_{c0}\cos(\beta)} \times \left[1 + \frac{\alpha^2}{4} + \frac{\tan(\beta)\alpha}{2}\left(e^{i\omega_m t+\phi} + e^{-i\omega_m t-\phi}\right) + \frac{\alpha^2}{8}\left(e^{2i\omega_m t+2\phi} + e^{-2i\omega_m t-2\phi}\right)\right]. \tag{18}$$

The first two terms in Eq. (18) are the dc-modulated and rf-modulated terms of the SQUID inductance, respectively. The third and fourth terms are the three-wave-mixing terms, which modulate $\omega \to \omega \pm \omega_m$. The fourth and fifth terms, the amplitude of which depends solely on the normalized rf drive strength α, give rise to four-wave mixing, which takes $\omega \to \omega \pm 2\omega_m$. These modulation tones can drive either amplification or frequency conversion processes, depending on their relation to the signal frequency. For the application in question, we will focus mainly on frequency conversion processes but note that this derivation can be generalized to either.

In the limit that the signal frequency $\omega' \gg \omega_m$, one can write the voltage-current relationship of a dc SQUID as

$$V(t) = L_{SQ}(t)\frac{dI(t)}{dt}, \tag{19}$$

where we have taken the current to be of the form $I(t) = I_0\exp[i\omega' t]$. Taking the Fourier transform $\mathcal{F}$ of both sides results in

$$\mathcal{F}\{V(t)\} = i\omega'\mathcal{F}\{L_{SQ}(t)\} * \mathcal{F}\{I(t)\}. \tag{20}$$

This results in a frequency domain voltage-current relationship given by

$$V(\omega) = L^0_{SQ}\left[\gamma\delta(\omega' - \omega) + \eta_+\delta(\omega' - \omega + 2\omega_m) + \eta_-\delta(\omega' - \omega - 2\omega_m)\kappa_+\delta(w' - \omega + \omega_m) + +\kappa_-\delta(\omega' - \omega - \omega_m)\right] * i\omega' I(\omega'), \tag{21a}$$

$$V(\omega) = i\omega L^0_{SQ}\gamma I(\omega) + i[\omega + 2\omega_m]L^0_{SQ}\eta_+ I(\omega + 2\omega_m) + i[\omega - 2\omega_m]L^0_{SQ}\eta_- I(\omega - 2\omega_m) + i[\omega + \omega_m]L^0_{SQ}\kappa_+ I(\omega + \omega_m) + i[\omega - \omega_m]L^0_{SQ}\kappa_- I(\omega - \omega_m), \tag{21b}$$

where $L^0_{SQ} = \Phi_0/4\pi I_{c0}\cos(\beta)$, $\gamma = 1 + \alpha^2/4$, $\eta_\pm = \alpha^2 e^{\pm i2\phi}/4$, and $\kappa_\pm = \tan(\beta)\alpha e^{\pm i\phi}/2$. The Dirac delta functions in Eq. (21a) form the connection between the signal and the sidebands produced from the mixing terms. From this, we can formulate the dc SQUID spectral impedance matrix $\mathbf{Z}_{SQ}$, where the voltage, current, and impedance are defined to account for $\pm 2\omega_m$ and $\pm\omega_m$ modulation products resulting from the Taylor expansion of Eq. (14):

$$\begin{bmatrix} V(\omega - 2\omega_m) \\ V(\omega - \omega_m) \\ V(\omega) \\ V(\omega + \omega_m) \\ V(\omega + 2\omega_m) \end{bmatrix} = \mathbf{Z}_{SQ}(\omega)\begin{bmatrix} I(\omega - 2\omega_m) \\ I(\omega - \omega_m) \\ I(\omega) \\ I(\omega + \omega_m) \\ I(\omega + 2\omega_m) \end{bmatrix}. \tag{22}$$

Equation (23) gives the spectral-impedance matrix $\mathbf{Z}_{SQ}(\omega)$ for a single dc SQUID [25], where $\omega_{n\pm} = \omega \pm n\omega_m$. Crucially, Eq. (23) demonstrates that the conversion amplitudes and associated phases between modulation products are *asymmetric* with respect to the conversion from one sideband to another:

$$\mathbf{Z}_{SQ}(\omega) = iL^0_{SQ}\times \begin{bmatrix} \gamma\omega_{2-} & \kappa_-\omega_{2-} & \eta_-\omega_{2-} & 0 & 0 \\ \kappa_+\omega_{1-} & \gamma\omega_{1-} & \kappa_-\omega_{1-} & \eta_-\omega_{1-} & 0 \\ \eta_+\omega & \kappa_+\omega & \gamma\omega & \kappa_-\omega & \eta_-\omega \\ 0 & \eta_+\omega_{1+} & \kappa_+\omega_{1+} & \gamma\omega_{1+} & \kappa_-\omega_{1+} \\ 0 & 0 & \eta_+\omega_{2+} & \kappa_+\omega_{2+} & \gamma\omega_{2+} \end{bmatrix}. \tag{23}$$

B. Two-port S parameters of a dc SQUID

With the spectral impedance matrix for a dc SQUID now defined, the scattering parameters of a shunted dc SQUID can be calculated. The basic circuit is illustrated in the inset of Fig. 2(a), where a dc SQUID under rf modulation is shunted to ground between two physical 50-Ω ports. These ports are coupled to the SQUID at all frequencies. The spectral ABCD matrix for a shunt dc SQUID is defined to be

$$\overline{\mathbf{A}}_{\mathrm{SQ}} \equiv \begin{bmatrix} \mathbf{A} & \mathbf{B} \\ \mathbf{C} & \mathbf{D} \end{bmatrix} = \begin{bmatrix} \mathbf{I}_n & \mathbf{0}_n \\ \mathbf{Z}_{\mathrm{SQ}}^{-1}(\omega) & \mathbf{I}_n \end{bmatrix}, \tag{24}$$

where $\mathbf{I}_n$ is the $n \times n$ identity matrix and $\mathbf{0}_n$ is a $n \times n$ matrix comprised of all zeroes. The resulting S parameters are then calculated as [8,26]

$$\mathbf{S}_{11} = \mathbf{I}_n - 2\left[\mathbf{I}_n + (\mathbf{A}Z_0 + \mathbf{B}) \times (\mathbf{C}Z_0^2 + \mathbf{D}Z_0)^{-1}\right]^{-1}, \tag{25a}$$

$$\mathbf{S}_{21} = 2\left[\mathbf{A} + \mathbf{B}/Z_0 + \mathbf{C}Z_0 + \mathbf{D}\right], \tag{25b}$$

$$\mathbf{S}_{12} = 2[\mathbf{I}_n + (\mathbf{A}Z_0 + \mathbf{B})(\mathbf{C}Z_0 + \mathbf{D})^{-1}/Z_0 \times (\mathbf{A} - (\mathbf{A}Z_0 + \mathbf{B})(\mathbf{C}Z_0 + \mathbf{D})^{-1}\mathbf{C}], \tag{25c}$$

$$\mathbf{S}_{22} = \mathbf{I}_n - 2\left[\mathbf{I}_n + (\mathbf{A}Z_0 + \mathbf{C}Z_0^2)^{-1} \times (\mathbf{B} + \mathbf{D}Z_0)\right]^{-1}, \tag{25d}$$

where each entry in the respective spectral S-parameter matrix is defined as

$$S_{ij}^{np} = \frac{b_i(\omega + n\omega_m)}{a_j(\omega + p\omega_m)}. \tag{26}$$

The terms b_i and a_j are the voltage waves entering and leaving ports i and j at their respective frequencies, defined by the indices n and p. Note that these S-parameter definitions are implicitly functions of the dc bias and rf modulation amplitudes applied to the dc SQUID and require recalculation at every bias point. We note that this definition is similar to what is discussed in Ref. [27] in the context of parametric circuits and elsewhere in the literature for nonlinear microwave devices in general.

We calculate the S parameters for a dc SQUID modulated at the pump tone frequency $\omega_m/2\pi = f_m = 500$ MHz with an rf signal tone $f_s = 7$ GHz. The critical current of the SQUID JJs is $I_{c0} = 5$ μA and the rf amplitude is $\alpha = 0.1\pi$. Figures 2(a) and 2(b) display the calculated S parameters in the three-wave ($\beta = 0.3\pi$) and four-wave ($\beta = 0$) mixing cases, respectively.

Having an imaginary admittance, the dc SQUID interrupts the impedance match between the ports, resulting in reduced transmission. However, the three- and four-wave mixing processes are clearly evident in the spectrum of transmitted and reflected S parameters. Figures 2(c) and 2(d) display the simulated first upper and lower sideband transmitted phases as a function of the modulation pump-tone phase for the three- and four-wave mixing cases, respectively. A well-defined dependency of the transmitted sideband tone phase on the pump tone phase can be clearly seen in both the three- and four-wave mixing cases. It is this phase dependency that we aim to utilize in a multi-SQUID architecture to achieve nonreciprocity.

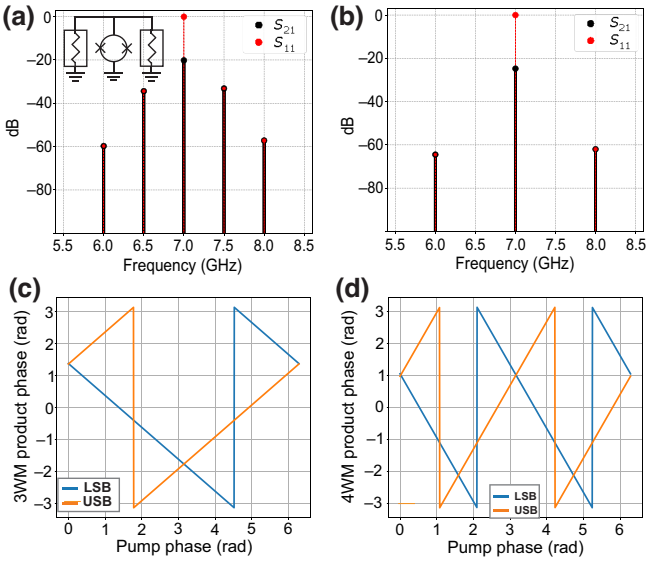

FIG. 2. (a) The forward and reflected scattering spectrum for a dc and rf flux biased dc SQUID with $\alpha = 0.1\pi$ and $\beta = 0.3\pi$ and a modulation frequency $\omega_m/2\pi = 500$ MHz. The inset shows the circuit diagram for the two-port dc SQUID calculation. (b) Forward and reflected scattering spectra for an rf flux biased dc SQUID with $\alpha = 0.1\pi$ and a modulation frequency of $\omega_m/2\pi = 500$ MHz. (c) The transmitted phase for the first three-wave mixing (3WM) upper and lower sideband as a function of the rf pump phase. (d) The transmitted phase for the first four-wave-mixing (4WM) upper and lower sideband as a function of the rf pump phase.

C. Generating directionality via the use of multiple SQUIDs

We further extend this model to the two dc SQUID circuit shown in the inset of Fig. 3. The circuit consists of two dc SQUIDs coupled by a series capacitor embedded on either side by 50-Ω ports. We calculate the measure of nonreciprocity of this circuit as the directionality D, defined as

$$D = |S_{21}^{00}|/|S_{12}^{00}|. \tag{27}$$

Each dc SQUID is driven at the same rf signal frequency ω_s and modulated with the same parameters shown in Fig. 2, with the exception of a differential phase, $\phi_d \equiv \phi_2 - \phi_1$, where ϕ_j is the phase of the rf tone applied to SQUID j.

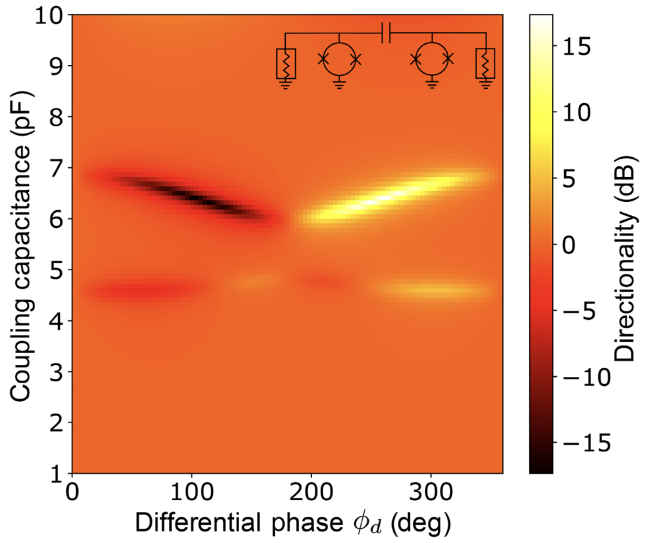

FIG. 3. The directionality of a circuit consisting of two dc SQUIDs coupled by a capacitor C embedded between two 50-Ω terminals. For the circuit schematic, see the inset. Each dc SQUID is modulated with the same parameters as in Fig. 2 with the exception of a differential phase, $\phi_d = \phi_2 - \phi_1$, between the applied tones. The plot displays the directionality D versus the differential phase and coupling capacitance. For specific values of C and ϕ_d, the directionality is nonzero. This illustrates that to achieve nonreciprocity, we need multiple (two or more) dc SQUIDS with a relative pump phase and an appropriate impedance coupling the dc SQUIDS.

The coupling capacitor is also varied as a way of sweeping the coupling impedance between the two dc SQUIDs. Figure 3 displays the directionality D as a function of ϕ_d and the coupling capacitance. It can be seen that the directionality is nonzero for particular sets of coupling capacitance values and phases.

When cascaded, The dc SQUIDs serve to mix the signal frequency to the upper and lower sidebands (as shown in Fig. 2) and back but with a phase offset all the while the coupling capacitance serves to couple and phase delay the remaining unmodulated signal frequency between ports. In tandem, these two processes can produce constructive or destructive interference, resulting in forward ($D > 1$) or reverse ($D < 1$) directionality. While this simple circuit shows that directionality can be achieved with as little as three circuit elements, without appropriate engineering of their values, a broadband match between the ports cannot be maintained. With this is mind, we have chosen to embed the SQUIDs into an admittance-inverting filter topology to allow for design flexibility.

D. ABCD harmonic balance results

A proposed multipole filter topology is illustrated in Fig. 4(a). It is a three-pole admittance-inverting filter, where the shunt inductor of each pole is replaced with a dc SQUID. The calculation of the implemented filter response is performed via cascading of the ABCD matrix for each admittance inverter and subsequent shunt LC pole. The forms of the spectral ABCD matrices are calculated following Ref. [8] and shown here for a dc SQUID. For a three-pole device, the ABCD matrix takes the form

$$\overline{\mathbf{A}}_{3P} = \begin{bmatrix} \frac{J_{34}J_{12}^2\mathbf{I}_n + J_{34}\overline{\mathbf{Y}}_{P1}\overline{\mathbf{Y}}_{P2}}{J_{01}J_{12}J_{23}} & \frac{J_{23}^2\overline{\mathbf{Y}}_{P1} + J_{23}^2\overline{\mathbf{Y}}_{P3} + \prod_{a=1}^{3}\overline{\mathbf{Y}}_{Pa}}{J_{12}J_{23}J_{34}} \\ \frac{J_{01}J_{34}\overline{\mathbf{Y}}_{P2}}{J_{12}J_{23}} & \frac{J_{01}J_{23}^2\mathbf{I}_n + J_{01}\overline{\mathbf{Y}}_{P2}\overline{\mathbf{Y}}_{P3}}{J_{12}J_{23}J_{34}} \end{bmatrix}. \tag{28}$$

We numerically calculate the response of a three-pole admittance-inverting filter under both quiescent dc flux bias and rf modulation conditions. We choose a Chebyshev filter response with center frequency $F_c = 7.3$ GHz, BW = 800 MHz, and in-band ripple $r_{\mathrm{dB}} = 0.125$ dB. The impedances of the three poles are set to 15, 10, and 15 Ω, respectively. For these simulations, we focus on the $\pm\omega_m$ and $\pm 2\omega_m$ modulation products. With the addition to the signal tone, this results in 5×5 spectral S-parameter matrices. Figure 4(a) displays a schematic of the simulated circuit. For no rf modulation and when biased at a value of $\beta = 0.3\pi$, the calculated response of the filter is that of a standard bandpass filter, as displayed in Fig. 4(b).

We calculate the circuit response again but now with each SQUID pumped at a common rf frequency and rf amplitude, but with differential phases. To verify the methodology, we compare the ABCD results with that of a numerical harmonic balance [28] simulation of the circuit. For the harmonic balance simulations, equivalent capacitive π-networks are substituted to implement the admittance inverters and a mathematically equivalent nonlinear model of the dc SQUID is utilized. In effort to capture the full nonlinearity of the dc SQUID, nine mixing orders in the signal and pump frequencies are utilized. Figure 4(c) displays the overlaid results of both the spectral ABCD matrix calculation and the harmonic balance simulation. For the spectral ABCD matrix calculation, $\beta = 0.3\pi, \alpha = 0.064\pi$ and a pump frequency $f_m =$ 691 MHz are used. The phases of the pumps are set to 0, $\pi/4$, and $\pi/2$, respectively. To achieve a matching response in the harmonic balance simulations, the pump frequency and rf pump amplitude had to be modified slightly to $f_m = 770$ MHz and $\alpha = 0.044\pi$, respectively. The modification of these parameters to achieve a phenomenologically matching response is expected as in the ABCD calculation, the dc SQUID nonlinearity is only expanded to second order. Higher orders of the applied flux $\mathcal{O}(\Phi_A^n)$, where $n > 2$, provide small but non-negligible alterations to the filter response that are more accurately captured in the harmonic balance simulations.

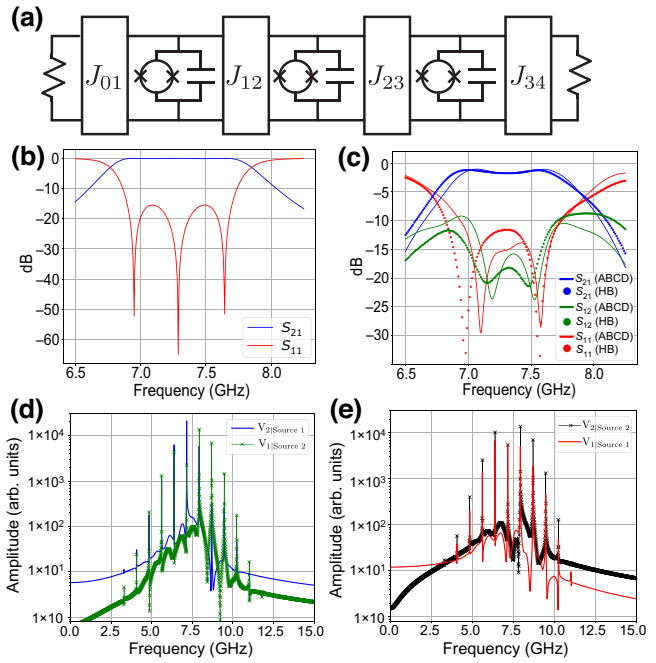

FIG. 4. (a) The three-pole admittance-inverting filter with dc SQUIDs as shunt inductors. The admittance inverters J_{XY} connect the modes of the filter and can be implemented as capacitor or inductor π networks or as 90° transmission lines. (b) The ABCD matrix calculated filter response with dc flux applied to each SQUID, with no rf modulation. (c) A comparison between the ABCD matrix calculation and harmonic balance simulation of the filter response with both dc bias and rf modulation of the dc SQUIDs. For the harmonic balance simulation, ideal inverters have been replaced with capacitive π-networks. With degenerate-frequency rf pumps applied to each of the three SQUIDs, tuning of the discrete phase differences between them can produce asymmetric transmission $|S_{21}^{00}(\omega)| \neq |S_{12}^{00}(\omega)|$. An important characteristic of this design is that the filter stays matched with an in-band return loss greater than 10 dB. (d) The calculated power spectra of the time-domain simulated transmitted voltage for the circuit in (a), driven at 7.150 GHz. When driving port 1 and measuring at port 2 ($V_{2|\text{Source 1}}$), the energy remains in the central frequency peak, while in the reverse operation ($V_{1|\text{Source 2}}$), the energy is dispersed into the three-wave mixing sidebands. (e) The calculated power spectra of the time domain simulated reflected voltage spectrum of the circuit in (a) when driven at 7.150 GHz.

We note again that the filter networks are employed to integrate the SQUIDs into a $Z = 50\Omega$ environment at dc flux bias *only* ($\alpha = 0$). From the previous treatment of the dc SQUID nonlinearity, when rf flux bias is applied ($\alpha \neq 0$), corrections to the bare SQUID inductance arise. However, this approximation of treating the circuit linearly to first couple and match the SQUIDs and treating the nonlinear modulation as a perturbation to that match allows us to separate the matching problem of the SQUIDs to both ports and the nonlinear modulation of the circuit. By choosing a topology that allows the overall circuit with the SQUID to remain matched, we can focus on optimizing the phase for nonreciprocal transmission, as shown in Sec. III. As shown in Fig. 4(c), this is a good design approximation. However, it is important to note that the rf flux bias does slightly degrade the filter match, effectively reducing the number of poles in the matching network (see Figs. 4(b) and 4(c)). We reserve the employment of more sophisticated matching networks to maintain the match while under rf modulation for future work and note that the incorporation of an additional matching network could have further improvement on the bandwidth and/or nonreciprocal behavior [19].

Figures 4(d) and 4(e) display the calculated power spectra derived from time-domain simulation results for the reflected- and transmitted-voltage spectra from the three-pole isolating filter at the signal frequency at 7.150 GHz, where the directionality is at a maximum. In the forward direction (drive port 1 and measure at port 2), the voltage is three-wave mixed from the carrier frequency and back, resulting in constructive interference and near-unity transmission. The additional insertion loss is due to the imperfect mode conversion back to the original signal frequency, resulting in residual voltage in the sidebands. This residual voltage is then either reflected back out of port 1 (Fig. 4(e), red curve) or transmitted through to port 2. In the reverse direction (drive port 2 and measure at port 1), the power at the signal mode is three-wave mixed *out of band* of the filter and reflected back out of port 2 (Fig. 4(e) black curve). Due to the combination of the finite roll-off of the filter and imperfect mode conversion, the achieved isolation is not infinite, with residual voltage at the signal frequency remaining unconverted and thus transmitted to port 1 with subsequent sidebands (Fig. 4(d), green curve).

Overall, the asymmetric transmission ratio at the signal frequency is maximized in the linear filter band. In general, the harmonic balance simulation and spectral S-parameter model show good agreement for both the transmitted and reflected S parameters at the signal frequency. While the harmonic balance model captures a more detailed picture of the nonlinear behavior of the dc SQUID, the good agreement shows that the physics of the circuit is well captured via the spectral S-parameter calculations, demonstrating that the lowest order modes dominate the response of the circuit when under modulation. Another important aspect of the device simulations is that they show that the device remains matched under rf modulation, with an in-band return loss greater than 10 dB.

IV. DESIGN AND FABRICATION

To experimentally verify the above theory, we fabricate two different circuit designs utilizing two- and three-pole filter structures, respectively. In each design, the impedance of the poles is determined so as to allow

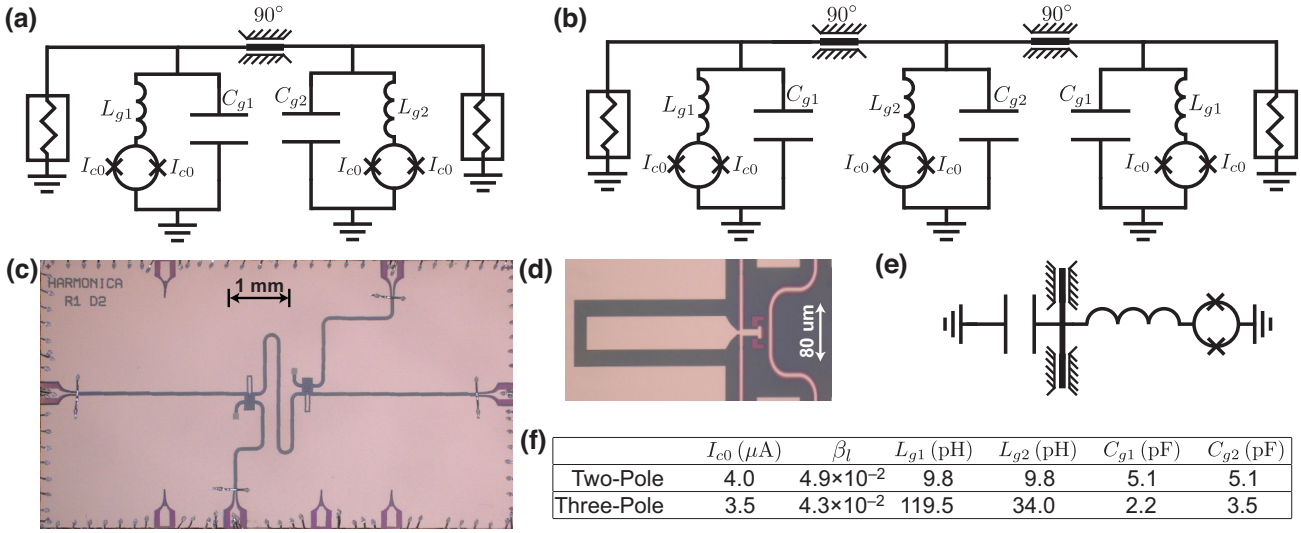

(f)

	I_{c0} (μA)	β_l	L_{g1} (pH)	L_{g2} (pH)	C_{g1} (pF)	C_{g2} (pF)
Two-Pole	4.0	4.9×10^{-2}	9.8	9.8	5.1	5.1
Three-Pole	3.5	4.3×10^{-2}	119.5	34.0	2.2	3.5

FIG. 5. (a) A schematic of the fabricated two-pole device. (b) A schematic of the fabricated three-pole device. (c) A micrograph of the two-pole device. (d) A micrograph of an *LC* pole shunt capacitor and dc SQUID. (e) A circuit schematic detailing the layout shown in (d). (f) Values for the circuit elements shown for the two- and three-pole devices in (a) and (b), respectively.

for $Z = 50\Omega, 90^\circ$ transmission-line couplers between the poles (for more details, see Appendix A). A common dc SQUID geometry is employed in all designs, with a geometric inductance of 12.8 pH as extracted with InductEx [29]. For each pole, a portion of the geometric shunt inductance is replaced by its flux biased dc SQUID equivalent, the proportion of which is numerically optimized to provide nominally identical critical currents in excess of $I_c > 1$ μA. The component parameters for the two devices are listed in Fig. 5(f). For the two-pole design, the poles are degenerate in their respective component values, while for the three-pole design, the first and third pole each employ the same component values, thus allowing for the geometric inductance and capacitance of poles one (L_{g1}/C_{g1}) and three (L_{g3}/C_{g3}) to be equal. Figures 5(a) and 5(b) display the schematics for the two- and three-pole circuit with the values for those respective circuit elements listed in Fig. 5(f).

The devices are fabricated utilizing a Nb trilayer process with a critical current density $J_c = 6$ μA/μm^2 [30]. The process is comprised of two superconducting metallic layers with an insulating tetraethyl orthosilicate (TEOS) SiO_x dielectric layer. The Nb base and counter electrode thicknesses are each 200 nm, with the interstitial SiO_x planarized to a thickness of 100 nm between the two metal layers. All layers are patterned atop a thermally oxidized silicon substrate. The base Nb layer serves as a ground plane for the circuit, while the second niobium layer allows for contact to the JJ counter electrode and additional on-chip wiring. A micrograph of the two-pole circuit is displayed in Fig. 5(c). Each dc SQUID has its own independent flux bias line (bottom left or top right), allowing for the application of dc and rf flux signals. An enlarged micrograph of an individual filter pole is presented in Fig. 5(d). The corresponding schematic detailing the parallel *LC* pole layout is shown in Fig. 5(e)

V. MEASUREMENTS

The packaged devices are loaded in a dilution refrigerator and thermally sunk to the mixing-chamber stage. Cryogenic through-reflect-line (TRL) [31] standards are implemented for coaxially deembedding the cabling, attenuation, and amplification between the vector network analyzer (VNA) and the device under test (DUT) up to the SMA cables of the devices. Because of the connector type (Ardent TR multicoax) used to connect the device package, approximately 18 in. of residual coaxial cable (flexible 047 coaxial cable) at either port is unable to be deembedded, along with the package printed circuit board (PCB) and wire bonds. The additional insertion losses from these elements are thus included in the measured insertion and return loss.

An experimental wiring diagram is included in Appendix B (see Fig. 10). The rf input lines to the TRL setup are attenuated at the 4 K and mixing chamber stages for a total of 66 dB of explicit attenuation at the input. The output amplification is provided via cryogenic low-noise amplifiers at the 4 K stage cascaded with low-noise amplifiers at room temperature. The flux biases are delivered via coaxial lines with 20 dB of attenuation at the 4 K stage and low-pass filtering at the MXC stage to protect the device from out-of-band noise. The room temperature signals are generated via dc sources (Yokogawa GS200) and rf sources (Holzworth HS900A) combined vias a bias

tee at room temperature. The device is characterized by a VNA (Keysight N5242B).

A. Two-pole isolating-filter response

The measured dc flux biased response of the filter with the accompanying harmonic balance simulation results are displayed in Fig. 6(a). An additional 2 dB of insertion loss is seen in the data when compared to the simulation. We attribute this difference to the imperfect calibration of the sample whereby the reference planes of the two-port calibration are offset from that of the sample planes by the additional coaxial cable, PCB traces, and wire bonds at either rf port (for an experimental wiring diagram, see Appendix B). Despite this limitation, there is still excellent agreement between the simulation and measured data both in terms of the bandwidth of the filter and the in-band return loss level.

The measured flux-pumped response of the two-pole isolating filter is shown in Fig. 6(b) along with the corresponding harmonic balance simulation of the device. The applied pump frequency is set to $f_m = 670$ MHz. Accounting for only the explicit attenuation in the flux line, the experimental rf flux pump amplitude $\alpha_E = 0.065\pi$. The shown simulation results utilize an rf flux pump amplitude $\alpha_S = 0.040\pi$. Again, we find excellent qualitative agreement between measurement and simulation. The difference in the maximum forward transmission between the measured and simulated responses is approximately 3 dB. The majority of this discrepancy can again be explained by the additional insertion loss from the physically offset calibration planes. We attribute the additional approximately 1 dB of insertion loss seen while rf pumping to higher-order inductance offset terms arising from the rf pump amplitude, which effects the impedance of the device. The phase offset between the two rf flux pumps in simulation is set to $\Delta\phi = 77.4^\circ$. Experimentally, the absolute phase difference between the pumps at chip level cannot be determined due to differing electrical lengths between the independent pump channels. The appropriate phase offset between the signals is determined experimentally.

Figures 6(c) and 6(d) display the measured forward and reverse scattering parameters of the two-pole device as a function of the differential phase offset. Figure 6(e) displays resulting vertical line cuts through Figs. 6(c) and 6(d) at $f = 7.2$ GHz. These data clearly show that the direction of power flow in the device can be set by adjusting the differential phase between the pumps, as predicted in Fig. 1(c).

B. Three-pole isolating-filter response

The measured and simulated responses for the three-pole device under quiescent dc flux bias and dc plus rf modulation are displayed in Figs. 7(a) and 7(b), respectively. Referring to Fig. 7(a), we see excellent agreement

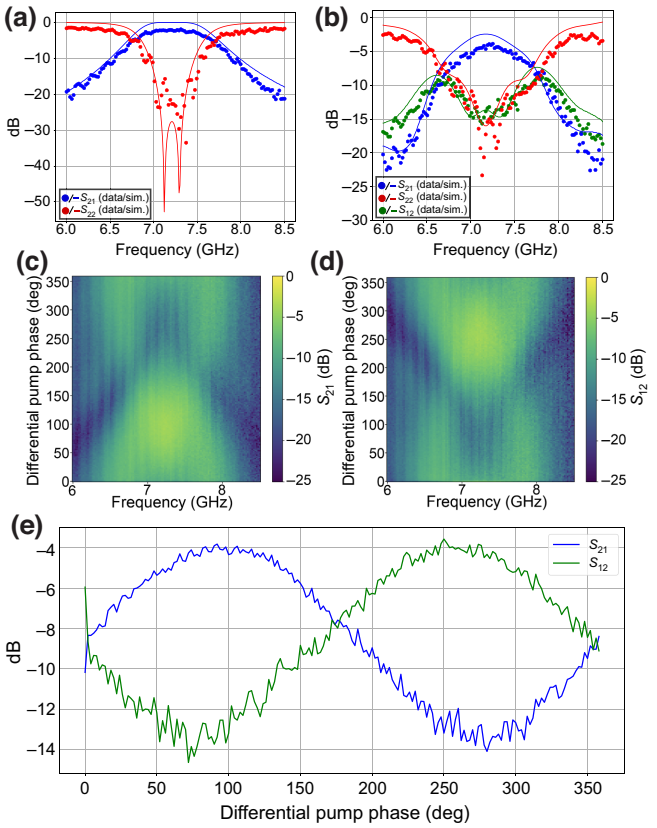

FIG. 6. (a) The simulated and measured response of the two-pole circuit at dc flux bias. (b) The simulated and measured response of the two-pole circuit under rf modulation of the dc SQUIDs. (c),(d) S_{21}^{00} and S_{12}^{00} as a function of the differential pump phase and the applied signal frequency. (e) Vertical line cuts of (c) and (d) at $f = 7.2$ GHz. The data show that by adjusting the differential pump phase between the two dc SQUIDs, the asymmetric transmission can be reversed from port 1 to port 2 and vice versa.

between the harmonic balance simulation and the measured data at quiescent dc flux bias. There is an approximately 2 dB discrepancy between the in-band through levels reported by the simulation and the measured data, which we again ascribe to the imperfect calibration mentioned earlier. The rf pumped isolating-filter response is displayed in Fig. 7(b), where the modulation tone is set to $f_m = 1100$ MHz. The estimated on-chip rf pump amplitude $\alpha_E = 0.078\pi$. The corresponding simulation is performed with a pump frequency $f_p = 1100$ MHz, a pump amplitude $\alpha_S = 0.09\pi$, and differential phases between the three pumps of 0°, 45.15°, and 88.57°, respectively. The phase offsets required to produce the measured spectrum are found experimentally. When properly set, we experimentally realize an isolating bandpass filter with an insertion loss IL < 5 dB and a directionality $D > 15$ dB over a bandwidth BW $= 600$ MHz. We note that the measured S_{11}^{00} degrades midband as compared to the simulation. However, the measured circuit does stay matched with a

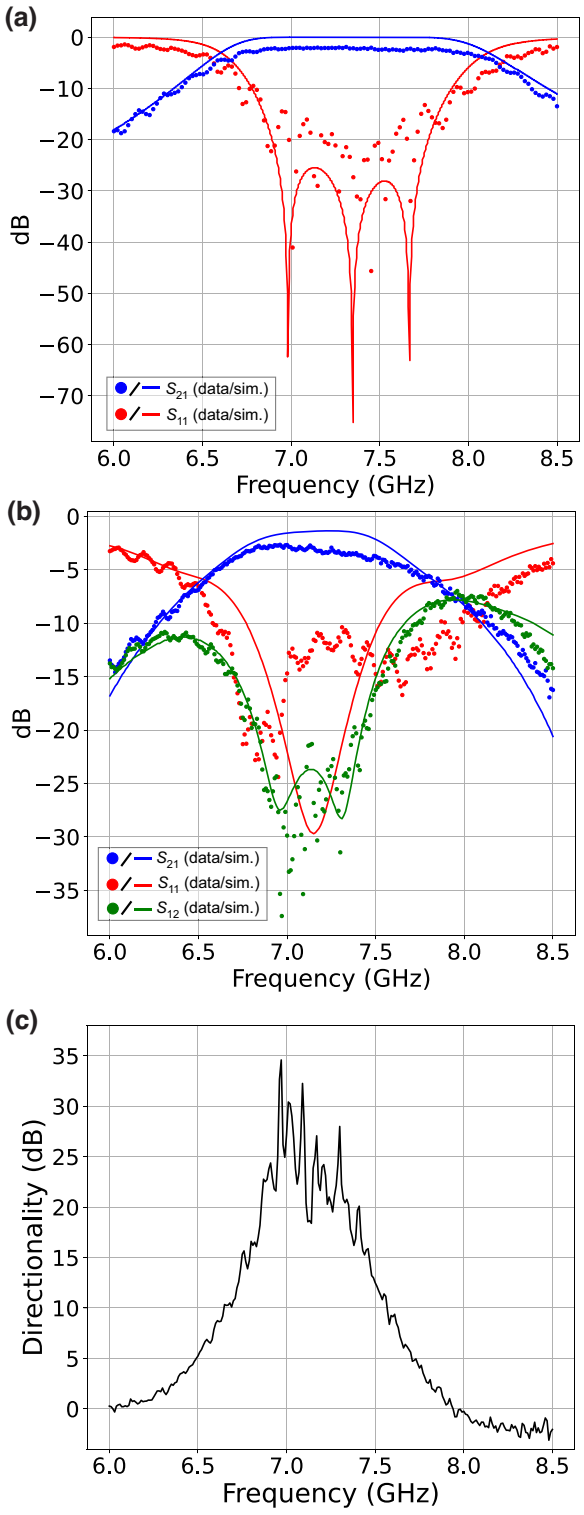

FIG. 7. (a) The measured and simulated responses for a three-pole filter at optimized dc flux bias. (b) The measured and simulated three-pole filter responses when pumped at $f_p = 1100$ MHz with differing phases between the pumps. The simulated response had differential phases between the three pumps of 0, 45.15°, and 88.57°, respectively. (c) The measured directionality $D = |S_{21}^{00}|/|S_{12}^{00}|$ of the three-pole isolating filter.

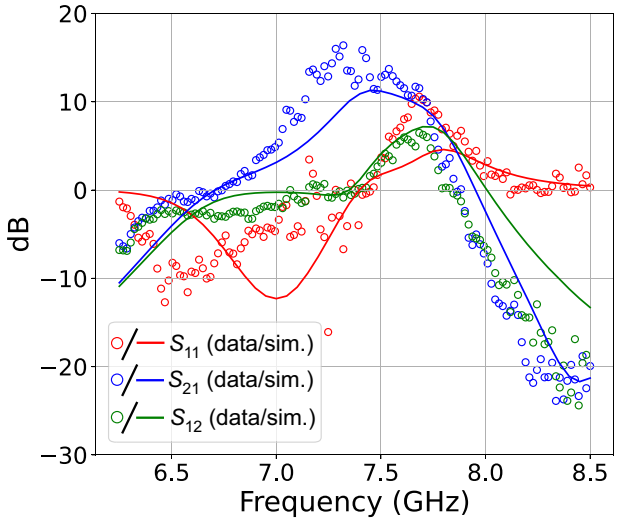

FIG. 8. The measured and simulated scattering parameters for the three-pole device when pumped at 14.69 GHz.

response better than −10 dB over the entire bandwidth. The directionality D of the device is plotted in Fig. 7(c) From 6.9 to 7.5 GHz, we achieve a directionality in excess of 15 dB.

C. Directional amplification

An independent mode of operation for the circuits described above is that of directional amplification. This mode is achieved by placing the pump frequency far above the center frequency of the passband: $f_m \gg f_c$. Setting $f_m = 2f_c$, the down-converted terms in the upper half of the impedance matrix in Eq. (23) develop a negative and real amplitude (for the proper pump phase) yielding the potential for gain. The key to achieving gain directionality is again the provision of two or more pumps with different phases such that the amplified idler modes can be mixed back to the signal mode constructively in one direction and destructively in the other.

To probe this mode of operation, we apply modulation tones of frequency $f_m = 14.69$ GHz to each SQUID of the three-pole device. The on-chip amplitude for each pump tone is calculated to be $\alpha_E = 0.099\pi$. The resulting measured and simulated frequency responses for S_{11}^{00} (red), S_{21}^{00} (blue), and S_{12}^{00} (green) are displayed in Fig. 8. Both theory and measurement demonstrate that the device remains passive in reflection ($S_{11}^{00} < 0$) up to 7.3 GHz, while simultaneously showing gain in the forward direction, which is a different mode of operation than that of traditional reflection-based amplifiers. With regard to the forward-scattering parameter S_{21}^{00}, we measure greater than 5 dB of gain over a bandwidth of BW ≈ 700 MHz, with a peak gain of 15 dB at 7.25 GHz. Conversely, $S_{12}^{00} < 0$ dB up

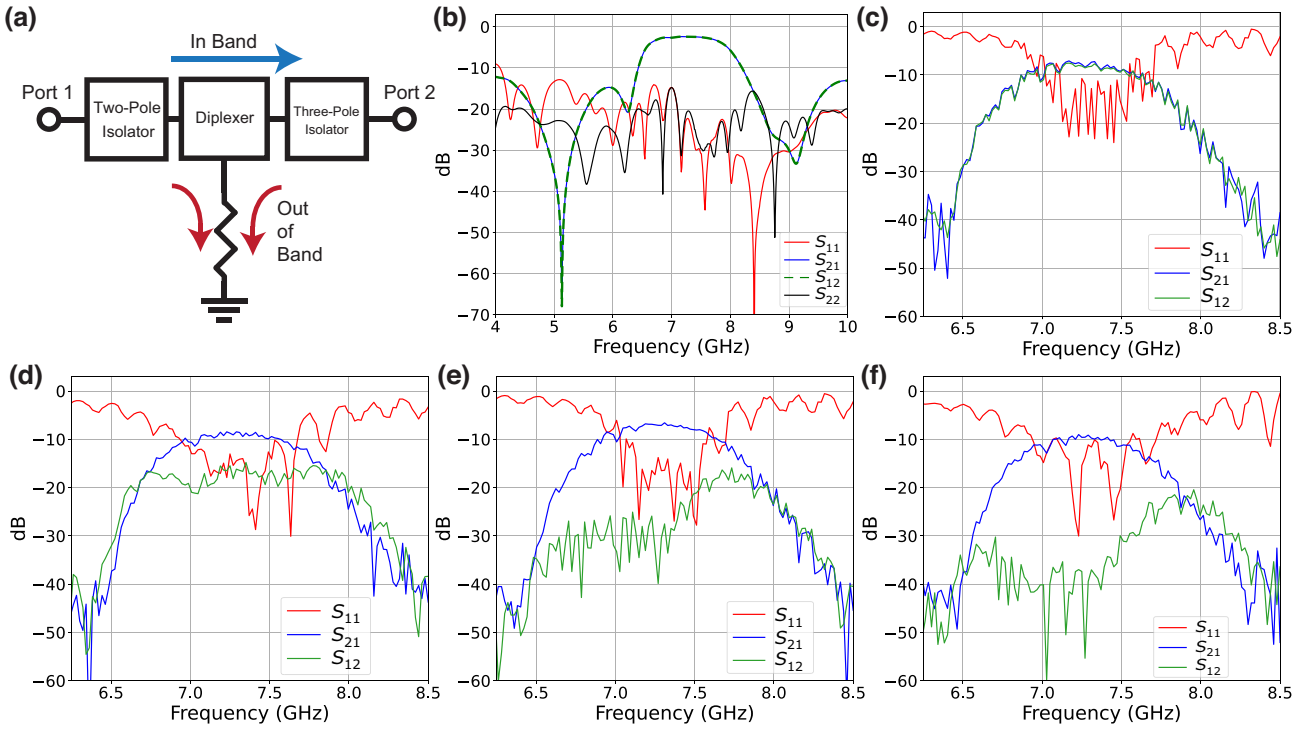

FIG. 9. (a) The circuit block diagram, detailing how the isolator devices are cascaded. (b) The measured room-temperature scattering parameters of the intermediate diplexer element at the ports used to connect the two isolator blocks. (c) The dc flux tuned-up cascaded isolators. The insertion loss of 8 dB is a combination of the insertion loss from the two filters and the diplexer plus an additional 72 inches of microwave cable that cannot be calibrated out of the measurement. (d) The cascaded isolator response with rf pumps applied solely to the two-pole device. (e) The cascaded isolator response with rf pumps applied solely to the three-pole device. (f) The cascaded-isolator response with rf pumps applied to both the two- and three-pole devices.

to approximately 7.4 GHz, after which we begin to measure reverse amplification between 7.4 and 7.9 GHz, with a maximum of 6 dB of gain at 7.7 GHz. In all measured parameters, we see very good model-hardware correlation.

We wish to emphasize here that the measurements of the amplifying capabilities of the circuit are done as a verification of the models. To achieve broadband directional amplification, further research, design, and development is required. With that, expansion into the calibration of standard amplifier specifications including added noise and saturation power is beyond the scope of this work.

D. Cascaded filters

With the demonstration of the two- and three-pole isolating filters above, an obvious future path toward increasing the directionality for a set bandwidth is to increase the number of poles. While we leave that direction for future exploration, it is worth noting some of the difficulties with that approach. Specifically, moving to an $n > 3$ pole-filter topology requires a more complicated device bring-up and operation. Specifically, beyond just considering fabrication variation, this includes dc bias-point optimization and static phase offsets at each dc SQUID that must be optimized and maintained across the device.

A notable way to alleviate this complexity is to cascade two or more multipole devices in an effort to achieve larger directionality. We highlight this approach for a few reasons. First, in comparison to building a more complex circuit, the operation of two cascaded circuits can result in a simpler bring-up. Each cascaded device can be brought up independently with respect to the dc bias and pump phase offsets. With little to no interplay between the respective biases and pumps between devices, the requirements on the phases of the pumps are simpler to implement. Further, cascading parametric devices is a critical path to achieving tightly integrated, small footprint readout electronics required for future quantum processors. Finally, in the absence of large environmental offsets or fabrication variation, identical devices, once cascaded, can ideally share the same bias and pump lines, thus significantly reducing the wiring overhead.

To demonstrate this idea, we present data obtained from experiments on the previously characterized two- and three-pole devices cascaded in series with an intermediate microwave diplexer. The basic experimental setup for these experiments is shown in Fig. 9(a). The

diplexer acts as an impedance match for the larger circuit across the full band of interest (including the stopband under linear operation). The diplexer performs the function of filtering out and directing the sidebands that arise from both the two-pole or three-pole device while under modulation into a 50-Ω termination while simultaneously allowing the signals in the passband to travel from port 1 to port 2. By filtering out generated sidebands between devices, we prevent any unwanted standing waves and allow for each device to be treated as an independent circuit. The diplexer is constructed using discrete commercial off-the-shelf components (Krytar Hybrid Coupler 3060200, Mini-circuit filters, VLF-6000+ and VHF-8400+, and cryogenic 50-Ω terminations from XMA Corporation). The S parameters of the diplexer, as measured at room temperature, are displayed in Fig. 9(b). We note that this passive circuit could be incorporated on chip or on package, with a small overhead in the overall design.

Figure 9(c) displays the S parameters for when both filters are biased with dc flux. The overall bandwidth is set by the two-pole filter. The best obtained insertion loss for the entire circuit is 8 dB. This insertion loss with respect to the calibration plane results from a combination of the insertion loss from the filters, the diplexer, and an additional 72 in. of microwave cable required to wire the experiment due to the connectors on both devices (Ardent TR multicoax). Both circuits are then tuned up independently for asymmetric transmission via application of rf flux to their respective *LC* poles. Figure 9(d) displays the isolating filter response when only the two-pole filter SQUIDs are pumped. The resulting directionality $D \approx 8\,\mathrm{dB}$ between 7.0 and 7.5 GHz. Figure 9(e) displays the cascaded-filter response with the rf pumps applied to the three-pole device SQUIDs. A directionality of $D \approx 20\,\mathrm{dB}$ is obtained with negligible additional insertion loss as compared to the nonmodulated response. Finally, the data when both isolators are pumped are presented in Fig. 9(f). The additive effect of the isolation of each filter is clearly seen in the suppression of S_{12} over the band from 7.0 to 7.5 GHz, ultimately reaching a directionality in excess of 25 dB. Crucially, in all modes of operation, the device remains matched in the band of interest, with an in-band return loss greater than 10 dB. The ability to cascade these parametric devices, despite their nonlinear mode of operation, allows for a straightforward method to incorporate these devices into a larger QPU readout chain.

VI. FUTURE OUTLOOK

The designs and the corresponding data presented above represent an initial step toward the realization of a superconducting integrated circuit replacement for traditional ferrite-based isolators. To continue this active area of research, future designs will have to address a few key issues seen with these initial devices. These issues are expanded upon below.

A. Increased directionality

The best directionality achieved in this work at a single frequency is approximately 30 dB. To replace modern commercial ferrite-based isolators, this level of directionality must be achieved across the entirety of the filter band. In order to accomplish this, two natural approaches are considered. The first and most straightforward approach is the simple cascading of multiple isolator devices in series. As shown above, for this to work properly, interstitial filters must be placed between the isolator stages to filter harmonics generated by the circuit. While easy to implement, this approach has drawbacks including, but not limited to, the requirement of additional lumped-element devices. These can, in theory, be integrated on chip without too much overhead. The second approach would be the inclusion of more poles in the filter design so as to allow for more pumps and thus more mixing control. The main drawback in this approach is that the number of high-bandwidth lines starts to become untenable. However, with the phases determined in advance from simulation, multiple pump lines could be combined in a single line with a deterministic phase delay implemented between sequential SQUIDS.

B. Decreased insertion loss

In terms of the readout requirements of QPUs, accumulating every measurement photon so as to maximize the quantum efficiency of the readout chain is extremely important [32]. Any device inserted in the readout chain that adds loss will naturally reduce the quantum efficiency. The pumped devices presented above show additional insertion loss when compared to their nonmodulated counterparts. For true integration, the insertion loss of these devices must be lowered. We reserve future work to explore more advanced methods in matching the SQUIDs not just at dc flux bias but while also under rf modulation.

C. Control-wiring overhead

For these initial demonstrations, each SQUID in this work is driven via its own independently controlled flux bias line. This allowed for experimental differential flux-offset compensation between all the SQUIDs and for the independent control of rf phases. For these devices to serve as viable alternative to current isolation devices, the flux-bias control wiring overhead should be considered as a hurdle to be overcome. A path toward achieving this is to engineer the circuit such that each dc SQUID requires a common dc flux offset such that a common line can be utilized. Further, the circuit and common line can then be engineered together such that, for the chosen

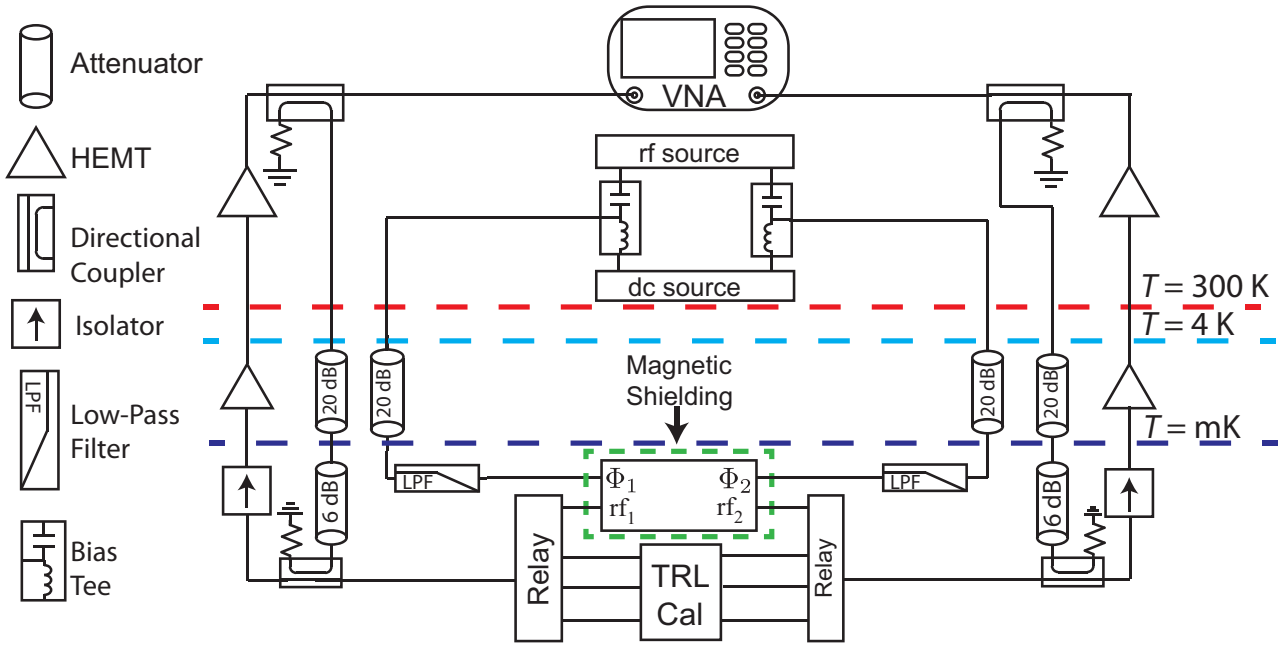

FIG. 10. The experimental wiring diagram for the isolator experiments. Here we show explicitly the wiring diagram for the two-pole device measurements. The experimental wiring is set such that the S parameter measurements can be calibrated both in transmission and reflection. One minor drawback is the inability to calibrate directly at the input and output planes of the DUT. This resulted in slighted increased insertion loss.

pump frequency, an appropriate electrical length between SQUIDs is allowed for.

VII. CONCLUSIONS

In summary, we have designed, modeled, and tested a two-port nonreciprocal device utilizing the three-wave mixing capabilities of dc SQUIDs embedded in multipole admittance inverting filters. Utilizing coupled-mode theory, we have extracted limitations on the pump frequency, pump phase, and pump amplitude so as to achieve nonreciprocity that describes well work published in the literature. We also provide a straightforward model that shows how three- and four-wave mixing arise from the inherent nonlinear inductance of a dc SQUID and can be utilized to realize nonreciprocal microwave transmission. This model has been further verified via harmonic balance simulations, where the full nonlinearity of the SQUID inductance could be more properly captured. These models show excellent agreement with measured data taken on two- and three-pole isolator devices, where we have achieved, over a bandwidth of 500 MHz, an in-band directionality of 8 and 15 dB, respectively. Further, we have shown with the three-pole device that directional amplification in excess of 10 dB over a 500 MHz BW can be achieved. Finally, we have presented measurements on the cascaded performance of a two- and three-pole isolating filter where a directionality approaching 30 dB has been obtained with minimal added insertion loss from the rf pumps.

Note added.—Recently, we have become aware of the work in Ref. [33], which reports on the use of a circuit using a modulated rf SQUID that can act as a circulator to achieve directionality in a 200-MHz band.

APPENDIX A: TRANSMISSION-LINE ADMITTANCE INVERTERS

The input admittance inverter J_{01} between a system impedance Z_0 and that of the first shunt LC resonator S_{r1} of a multipole filter has the form

$$J_{01} = \sqrt{\frac{\overline{\omega}}{g_0 g_1 Z_0 Z_{r1}}}, \tag{A1}$$

where $\overline{\omega} = (\omega_2 - \omega_1)/\sqrt{\omega_2\omega_1}$, in which ω_1 and ω_2 are the lower and upper knee frequencies of the filter, and g_0 and g_1 are the first two terms in the lowpass filter coefficients. By explicitly setting $J_{01} = 1/Z_0$ and solving for $Z_{r,1}$, one arrives at

$$Z_{r,1} = \frac{\overline{\omega} Z_0}{g_0 g_1}. \tag{A2}$$

This is the impedance to which one must set the first LC resonator of the filter in order to allow for a direct Z_0

input to the filter with no explicit inverter structure. For completeness, we also show how one designs the inter-resonator coupling to also be Z_0. The form of the interpole admittance inverter is between poles n and $n+1$ is defined as

$$J_{n,n+1} = \overline{\omega}\sqrt{\frac{1}{g_n g_{n+1} Z_{r,n} Z_{r,n+1}}}. \tag{A3}$$

Again, we set the admittance value $J_{n,n+1} = 1/Z_0$ and solve for $Z_{r,n+1}$, yielding

$$Z_{r,n+1} = \frac{Z_0^2 \overline{\omega}^2}{g_n g_{n+1} Z_{r,n}}. \tag{A4}$$

Taking $n = 1$ and the result of Eq. (A2), we can reduce Eq. (A4) to

$$Z_{r,2} = \frac{Z_0^2 \overline{\omega}^2}{g_1 g_2 Z_{r,1}} \tag{A5a}$$

$$= \frac{Z_0^2 \overline{\omega}^2}{g_1 g_2 \frac{\overline{\omega} Z_0}{g_0 g_1}} \tag{A5b}$$

$$= \frac{Z_0 \overline{\omega} g_0}{g_2}. \tag{A5c}$$

The process outlined above can be continued to fully determine the impedance of every LC network in the filter once a filter type, center frequency, bandwidth, and ripple have been determined.

While the above treatment provides a method of determining the required impedance of each of the LC poles coupled via a transmission line of impedance Z_0, we note here that this treatment alone is not entirely sufficient, as the electrical length of the transmission line must be explicitly defined. To calculate the appropriate electrical length of the transmission line, we reproduce here the form of the input impedance of a transmission line Z_0 connected to a load of impedance Z_L [34]:

$$Z_{\text{in}} = Z_0 \frac{Z_L + iZ_0 \tan(\kappa l)}{Z_0 + iZ_L \tan(\kappa l)}, \tag{A6}$$

where $\kappa = 2\pi/\lambda$ is the wave number, λ is the wavelength, and l is the electrical length of the transmission line. In the limit that $l \to \lambda/4$, the terms proportional to $\tan(\kappa l)$ begin to diverge, simplifying Eq. (A6) to

$$Z_{\text{in}} = \frac{Z_0^2}{Z_L}. \tag{A7}$$

Taking the simple transformations $Z_{\text{in}} = 1/Y_{\text{in}}$, $Z_0 = 1/Y_0$, and $Z_L = 1/Y_L$, we arrive at

$$Y_{\text{in}} = \frac{Y_0^2}{Y_L}. \tag{A8}$$

APPENDIX B: EXPERIMENTAL WIRING

Figure 10 displays the experimental wiring utilized for the measurement of two-pole sample data. When measuring for the three-pole sample, an extra rf and dc source channel along with a bias tee is required. Channels 1 and 2 from the VNA are split via directional couplers such that the transmission and reflection scattering parameters could be calibrated *in situ*.

A minor drawback in this experimental setup is the inability to calibrate directly up to the input and output planes of the DUT. This experimental constraint manifests itself in measurement as an additive insertion loss in both the forward- and reverse-scattering parameters, stemming from the cabling between the relays and the rf channels of the DUTs.

[1] A. Wallraff, D. I. Schuster, A. Blais, L. Frunzio, J. Majer, M. H. Devoret, S. M. Girvin, and R. J. Schoelkopf, Approaching Unit Visibility for Control of a Superconducting Qubit with Dispersive Readout, Phys. Rev. Lett. **95**, 060501 (2005).

[2] Y. Chen, D. Sank, P. O'Malley, T. White, R. Barends, B. Chiaro, J. Kelly, E. Lucero, M. Mariantoni, A. Megrant, C. Neill, A. Vainsencher, J. Wenner, Y. Yin, A. N. Cleland, and J. M. Martinis, Multiplexed dispersive readout of superconducting phase qubits, App. Phys. Lett. **101**, 182601 (2012).

[3] T. Walter, P. Kurpiers, S. Gasparinetti, P. Magnard, A. Potočnik, Y. Salathé, M. Pechal, M. Mondal, M. Oppliger, C. Eichler, and A. Wallraff, Rapid High-Fidelity Single-Shot Dispersive Readout of Superconducting Qubits, Phys. Rev. Appl. **7**, 054020 (2017).

[4] C. Neill, *et al.*, A blueprint for demonstrating quantum supremacy with superconducting qubits, Science **360**, 195 (2018).

[5] E. J. Zhang, *et al.*, High-performance superconducting quantum processors via laser annealing of transmon qubits, Sci. Adv. **8**, 19 (2022).

[6] M. Boissonneault, J. M. Gambetta, and A. Blais, Dispersive regime of circuit QED: Photon-dependent qubit dephasing and relaxation rates, Phys. Rev. A **79**, 013819 (2009).

[7] E. I. Rosenthal, C. M. F. Schneider, M. Malnou, Z. Zhao, F. Leditzky, B. J. Chapman, W. Wustmann, X. Ma, D. A. Palken, M. F. Zanner, L. R. Vale, G. C. Hilton, J. Gao, G. Smith, G. Kirchmair, and K. W. Lehnert, Efficient and Low-Backaction Quantum Measurement Using a Chip-Scale Detector, Phys. Rev. Lett. **126**, 090503 (2021).

[8] X. Wu, X. Liu, M. D. Hickle, D. Peroulis, J. S. Gómez-Díaz, and A. Á. Melcón, Isolating bandpass filters using time-modulated resonators, IEEE. Trans. Microw. Theory Tech. **67**, 2331 (2019).

[9] L. Ranzani, S. Kotler, A. J. Sirois, M. P. DeFeo, M. Castellanos-Beltran, K. Cicak, L. R. Vale, and J. Aumentado, Wideband Isolation by Frequency Conversion in a Josephson-Junction Transmission Line, Phys. Rev. Appl. **8**, 054035 (2017).

[10] F. Lecocq, L. Ranzani, G. A. Peterson, K. Cicak, R. W. Simmonds, J. D. Teufel, and J. Aumentado, Nonreciprocal Microwave Signal Processing with a Field-Programmable Josephson Amplifier, Phys. Rev. Appl. **7**, 024028 (2017).

[11] B. Abdo, N. T. Bronn, O. Jinka, S. Olivadese, A. D. Córcoles, V. P. Adiga, M. Brink, R. E. Lake, X. Wu, D. P. Pappas, and J. M. Chow, Active protection of a superconducting qubit with an interferometric Josephson isolator, Nat. Commun. **10**, 3154 (2019).

[12] B. Abdo, O. Jinka, N. T. Bronn, S. Olivadese, and M. Brink, High-Fidelity Qubit Readout Using Interferometric Directional Josephson Devices, PRX Quantum **2**, 040360 (2021).

[13] T. C. Chien, O. Lanes, C. Liu, X. Cao, P. Lu, S. Motz, G. Liu, D. Pekker, and M. Hatridge, Multiparametric amplification and qubit measurement with a Kerr-free Josephson ring modulator, Phys. Rev. A **101**, 042336 (2020).

[14] K. M. Sliwa, M. Hatridge, A. Narla, S. Shankar, L. Frunzio, R. J. Schoelkopf, and M. H. Devoret, Reconfigurable Josephson Circulator/Directional Amplifier, Phys. Rev. X **5**, 041020 (2015).

[15] D. Zhang and J.-S. Tsai, Magnetic-Free Traveling-Wave Nonreciprocal Superconducting Microwave Components, Phys. Rev. Appl. **15**, 064013 (2021).

[16] M. Naghiloo, K. Peng, Y. Ye, G. Cunningham, and K. P. O'Brien, Broadband microwave isolation with adiabatic mode conversion in coupled superconducting transmission lines, ArXiv:2103.07793 (2021).

[17] B. J. Chapman, E. I. Rosenthal, J. Kerckhoff, B. A. Moores, L. R. Vale, J. A. B. Mates, G. C. Hilton, K. Lalumière, A. Blais, and K. W. Lehnert, Widely Tunable On-Chip Microwave Circulator for Superconducting Quantum Circuits, Phys. Rev. X **7**, 041043 (2017).

[18] L. Ranzani and J. Aumentado, Graph-based analysis of nonreciprocity in coupled-mode systems, New. J. Phys. **17**, 023024 (2015).

[19] O. Naaman and J. Aumentado, Synthesis of Parametrically Coupled Networks, PRX Quantum **3**, 020201 (2022).

[20] O. Naaman, M. O. Abutaleb, C. Kirby, and M. Rennie, On-chip Josephson junction microwave switch, App. Phys. Lett. **108**, 112601 (2016).

[21] O. Naaman, D. G. Ferguson, A. Marakov, M. Khalil, W. F. Koehl, and R. J. Epstein, in *2019 IEEE MTT-S International Microwave Symposium (IMS)* (2019), p. 259.

[22] O. Naaman, J. A. Strong, D. G. Ferguson, J. Egan, N. Bailey, and R. T. Hinkey, Josephson junction microwave modulators for qubit control, J. Appl. Phys. **121**, 073904 (2017).

[23] A. Alvarez-Melcon, X. Wu, J. Zang, X. Liu, and J. S. Gomez-Diaz, Coupling matrix representation of nonreciprocal filters based on time-modulated resonators, IEEE. Trans. Microw. Theory Tech. **67**, 4751 (2019).

[24] R. Cantor and D. Koelle, in *The SQUID Handbook* (Wiley-VCH, 2004), p. 171.

[25] K. M. Sundqvist and P. Delsing, Negative-resistance models for parametrically flux-pumped superconducting quantum interference devices, EPJ Quantum Technol. **1**, 6 (2014).

[26] J. B. Faria, *Multiconductor Transmission-Line Structures* (John Wiley and Sons, New York, NY, 1993).

[27] K. Peng, R. Poore, P. Krantz, D. E. Root, and K. P. O'Brien, X-parameter based design and simulation of Josephson traveling-wave parametric amplifiers for quantum computing applications, ArXiv:2211.05328 (2022).

[28] R. J. Gilmore and M. B. Steer, Nonlinear circuit analysis using the method of harmonic balance—a review of the art. Part I. Introductory concepts, Int. J. Microw. Millim.-Wave Comput.-Aided Eng. **1**, 22 (1991).

[29] C. J. Fourie, O. Wetzstein, T. Ortlepp, and J. Kunert, Three-dimensional multi-terminal superconductive integrated circuit inductance extraction, Supercond. Sci. Technol. **24**, 125015 (2011).

[30] Z. Cui, J. R. Kirtley, Y. Wang, P. A. Kratz, A. J. Rosenberg, C. A. Watson, G. W. Gibson, M. B. Ketchen, and K. A. Moler, Scanning squid sampler with 40-ps time resolution, Rev. Sci. Instrum. **88**, 083703 (2017).

[31] L. Ranzani, L. Spietz, Z. Popovic, and J. Aumentado, Two-port microwave calibration at millikelvin temperatures, Rev. Sci. Instrum. **84**, 034704 (2013).

[32] C. C. Bultink, B. Tarasinski, N. Haandbæk, S. Poletto, N. Haider, D. J. Michalak, A. Bruno, and L. DiCarlo, General method for extracting the quantum efficiency of dispersive qubit readout in circuit QED, App. Phys. Lett. **112**, 092601 (2018).

[33] R. Kwende, T. White, and O. Naaman, Josephson parametric circulator with same-frequency signal ports, 200 MHz bandwidth, and high dynamic range, ArXiv:2303.06757 (2023).

[34] D. M. Pozar, *Microwave Engineering* (John Wiley and Sons, Hoboken, NJ, 2005), 3rd ed.